JOURNAL OF APPLIED PHYSICS **99**, 083103 (2006)

Fabrication and characterization of erbium-doped toroidal microcavity lasers

J. Kalkman,[a] A. Tchebotareva, and A. Polman[b]
Center for Nanophotonics, FOM Institute AMOLF, Kruislaan 407, 1098 SJ Amsterdam, The Netherlands

T. J. Kippenberg, B. Min, and K. J. Vahala[c]
California Institute of Technology, Pasadena, California 91125

(Received 8 June 2005; accepted 22 February 2006; published online 27 April 2006)

Erbium-doped SiO_2 toroidal microcavity lasers are fabricated on a Si substrate using a combination of optical lithography, etching, Er ion implantation, and CO_2 laser reflow. Erbium is either preimplanted in the SiO_2 base material or postimplanted into a fully fabricated microtoroid. Three-dimensional infrared confocal photoluminescence spectroscopy imaging is used to determine the spatial distribution of optically active Er ions in the two types of microtoroids, and distinct differences are found. Microprobe Rutherford backscattering spectrometry indicates that no macroscopic Er diffusion occurs during the laser reflow for preimplanted microtoroids. From the measured Er doping profiles and calculated optical mode distributions the overlap factor between the Er distribution and mode profile is calculated: $\Gamma=0.066$ and $\Gamma=0.02$ for postimplanted and preimplanted microtoroids, respectively. Single and multimode lasing around 1.5 μm is observed for both types of microtoroids, with the lowest lasing threshold (4.5 μW) observed for the preimplanted microtoroids, which possess the smallest mode volume. When excited in the proper geometry, a clear mode spectrum is observed superimposed on the Er spontaneous emission spectrum. This result indicates the coupling of Er ions to cavity modes. © *2006 American Institute of Physics*. [DOI: 10.1063/1.2188050]

I. INTRODUCTION

Optical microcavities are dielectric microstructures that confine light both spatially and temporally. They are ideal platforms to study cavity quantum electrodynamical effects, enhanced or suppressed spontaneous emission, and can be applied in devices such as low-threshold lasers, optical filters, wavelength multiplexers, and optical memories.[1,2] The figure of merit that describes the cavity is the quality factor Q that is proportional to the photon storage time $\tau=Q/\omega$, with ω as the angular frequency. Planar ring resonator structures have been fabricated with Q up to 1.3×10^5.[3] More recently, photonic crystal microcavities with $Q=1.3\times10^4$ have been demonstrated.[4] The highest cavity Q's, larger than 10^9, have been measured on whispering gallery mode optical resonators based on silica microspheres.[5–8] While interesting because of their ultrahigh Q, these microspheres are difficult for use in actual photonic devices because they are fragile and cannot be easily integrated on a Si substrate.

Recently, a process for the fabrication of silica microcavities on a planar substrate was developed that is compatible with Si-integrated-circuit manufacturing.[9] It involves standard fabrication processes combined with a laser reflow process that results in silica toroidal ring resonators on a Si substrate with $Q>10^8$. Light is coupled into these cavities using a tapered optical fiber. Due to the high optical field intensities that can be achieved in these high-Q microcavities, low-threshold lasing[10] and nonlinear effects have been demonstrated.[11,12]

In this paper we describe the doping of these Si-chip based resonators with Er ions, and show the realization of an on-chip Er microlaser. Ion implantation is used as the doping technique since it gives control over the doping profile and composition, and is compatible with Si-integrated-circuit manufacturing. We compare two different fabrication methods, one where Er-implanted SiO_2 is used as the starting material from which a microtoroid is subsequently made, and one where the Er is implanted in a fully fabricated microtoroid. We use confocal photoluminescence (PL) spectroscopy and microprobe Rutherford backscattering spectrometry (μRBS) to determine the Er distribution for two microtoroid Er doping procedures. Er lasing is observed in both types of Er-doped microcavities and the lasing characteristics are compared.

II. EXPERIMENTAL TECHNIQUES

A. Fabrication of Er-doped microtoroids

Fabrication of microtoroids was carried out as follows (see Fig. 1, described in Ref. 9). The starting material is a 1–2 μm thick layer of thermally grown SiO_2 on a Si substrate (step 1). Next, a photoresist is spin coated onto the sample (step 2). Using optical lithography, circular structures are defined in the photoresist, which, after development, leave circular patches of photoresist (step 3). The circular patches are then transferred into the SiO_2 by wet-chemical etching in HF (step 4). The remaining photoresist is removed

[a]Electronic mail: jeroenkalkman@philips.com
[b]Electronic mail: polman@amolf.nl
[c]Electronic mail: vahala@caltech.edu

 © 2006 American Institute of Physics

Downloaded 12 Jun 2006 to 192.87.154.163. Redistribution subject to AIP license or copyright, see http://jap.aip.org/jap/copyright.jsp

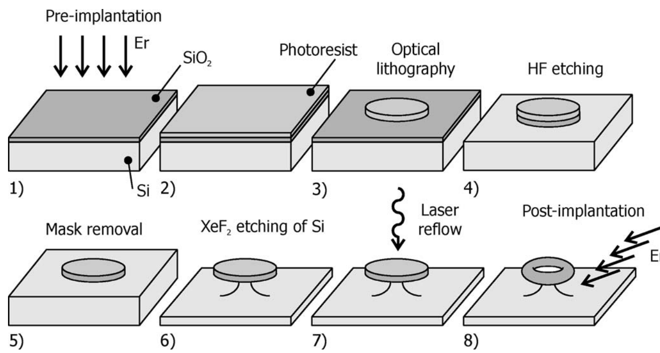

FIG. 1. Fabrication process of Er-doped ultrahigh-Q microtoroids [after (Ref. 9)]. Er doping is done by ion implantation at step 1 or 8.

with acetone (step 5). Using a XeF_2 gas etch, the Si is isotropically etched, leaving a circular SiO_2 disk on a Si post (step 6). Finally, these disks are transformed into microtoroids by a CO_2 laser pulse (10 W, 1 ms) (step 7). Figure 2 shows a scanning electron microscopy (SEM) image of a typical fabricated microtoroid. Erbium doping of these microtoroids is performed in two ways. In the first method, a toroidal microcavity on a chip is fabricated first by the above-described steps and is then implanted with Er ions in step 8 ("postimplanted" microtoroid). Since the optical mode resides at the outer edge of the toroidal periphery, the microtoroid was implanted from the side. In this way a known but inhomogeneous (not cylindrically symmetric) implantation profile is obtained, which exhibits good overlap with the optical modes. In the second method, Er ions are implanted in the SiO_2 base material (step 1) that is subsequently processed into a toroidal microcavity ("preimplanted" microtoroid). While the latter procedure is more compatible with standard fabrication processes and leads to a higher throughput, the subsequent laser reflow has a significant effect on the Er distribution as we shall show later.

Postimplanted microtoroids were made in the following way. Arrays of 35 freshly prepared microtoroids on a single chip with diameters of around 60 μm were fabricated. Directly after fabrication it was verified that their Q's were larger than 10^8. The Si-chip sample was then mounted on a 70° wedge, attached to a Si wafer. In this way Er ions are implanted at an angle of 70° relative to the toroid's axis of symmetry (see Fig. 1), which results in an Er distribution that has good overlap with the high-Q optical modes of the

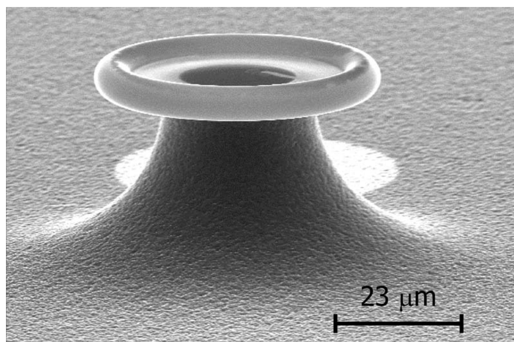

FIG. 2. Scanning electron micrograph of a typical postimplanted microtoroid. Note the implantation "shadow" behind the microtoroid.

microtoroid. The sample is subsequently implanted with 2 MeV Er^+ at a fluence of 4.2×10^{15} cm^{-2}. The Er implantation depth profile is calculated with TRIM,[13] a Monte Carlo simulation program. It is Gaussian shaped, peaking at a depth of 596 nm with a peak concentration of 0.2 at. %. The sample is then thermally annealed for 1 h at 800 °C in vacuum. An oxygen plasma etch was applied to remove carbon contamination from the surface of the microtoroid (caused by the ion implantation process in some cases). Figure 2 shows a SEM image of a postimplanted microtoroid with a" shadow" imprint of the ion beam clearly visible in the background.

Preimplanted microtoroids were made using samples with 1 or 2 μm thick thermally grown SiO_2 films on a Si substrate. The 2 μm thick SiO_2 was implanted with 2 MeV Er^+ ions at a fluence of either 4.2×10^{15} or 1.2×10^{16} cm^{-2}. The Er projected range is R_p=596 nm, with a peak concentration of 0.2 or 0.65 at. %. The 1 μm thick SiO_2 was implanted with 300 keV Er^+ at a fluence of 2.8×10^{15} cm^{-2}. This leads to a shallower Er profile (R_p=110 nm), with a peak concentration of 0.7 at. %. Finally, toroidal microresonators were fabricated from the Er-implanted oxide layers, (preimplanted) using the method described above.

B. Time-resolved and confocal photoluminescence spectroscopy

Time-resolved infrared PL spectroscopy was performed using lock-in amplification in combination with a time-modulated Ar ion laser, 480 mm monochromator, and a liquid-nitrogen cooled Ge diode detector. The laser spot diameter was ~500 μm and thus covered an entire microresonator structure so that PL spectra and lifetimes averaged over the entire structure were measured. A high-magnification charge-coupled device (CCD) camera was employed to position the laser spot on a particular microdisk or microtoroid structure on the Si-chip sample.

Spatially resolved PL spectroscopy was done with a scanning confocal microscope (WITec GmbH, Germany). As an excitation source we used a frequency-doubled Nd-YAG (trium aluminum garnet) laser operating at a wavelength of 532 nm of which the output was coupled into an optical fiber that was fed into the microscope. The laser beam is directed onto the sample using an infrared beamsplitter and is focused using either a 60×(NA=0.8) objective (air) or a plan apochromatic 100× oil immersion objective (NA=1.4). High-resolution images were obtained using index matching. The microtoroid sample was enclosed in a small chamber filled with index matching oil (n=1.52) and covered with a 170 μm thick silica glass cover slide. This assembly was then imaged using the same oil between objective and sample. While index matching does provide the highest possible spatial resolution, it makes it impossible to locate the toroidal perimeter in the images. To enable direct comparison between PL images and the toroidal volume, the immersion oil was lightly doped with Rhodamine dye (emission maximum at λ=545 nm). The dye preferentially absorbs on the microtoroid's surface and its luminescence was used to probe the microtoroid's outer contours. The infrared Er PL is col-

Downloaded 12 Jun 2006 to 192.87.154.163. Redistribution subject to AIP license or copyright, see http://jap.aip.org/jap/copyright.jsp

lected via the same objective and fed into an optical fiber with a 100 μm core that is located in the image plane, and acts as the confocal detection pinhole. The PL is then dispersed with a 300 mm monochromator with a resolution of 0.1 nm and imaged onto either a Si CCD detector operating in the visible ($\lambda = 350-900$ nm) or an InGaAs infrared array detector ($\lambda = 800-1700$ nm). The sample is scanned in either the *x-y* or the *x-z* plane of the toroidal structure, while at every point of the scan a PL spectrum is recorded. Spatial PL intensity distributions are obtained by integrating a spectral region of the measured spectrum. Using a reference sample coated with a thin dye layer the resolution in the *z* direction at $\lambda = 580$ nm was measured to be ~ 800 nm. At $\lambda = 1500$ nm a resolution of ~ 2 μm is expected. The lateral resolution in the *x* and *y* directions is expected to be somewhat higher.

C. Microprobe Rutherford backscattering spectrometry

Microprobe Rutherford backscattering spectrometry was performed to determine the Er depth profile inside the microtoroids. We used a High-Voltage Engineering singletron ion accelerator with a 2 MeV He^+ microprobe beam. A passivated implanted planar silicon detector mounted at 147° relative to the incident beam was used to detect backscattered He^+ ions. Simultaneously, the particle-induced x-ray emission (PIXE) was detected using a liquid-nitrogen cooled Ge detector. The circularly shaped He^+ beam (2.5 μm diameter) was scanned over the sample area at a rate of 1 kHz. The beam current at the sample was 200 pA, as measured with a Faraday cup located at the entrance of the scattering chamber.

D. Fiber coupling to microtoroids

The quality factors of the Er-implanted microtoroids were determined by measuring the transmission spectrum of a tapered optical fiber brought in close proximity to a microresonator. We used a tunable narrow-linewidth external-cavity diode laser (1400–1500 nm) that was fed into the tapered optical fiber. The laser scanning speed was chosen sufficiently low, so that at each frequency the mode intensity and the Er population reach a steady state. The tapered optical fiber is mounted on a high-precision piezoelectric stage (step resolution of 20 nm). At a fixed distance from the microtoroid a transmission spectrum is measured by scanning the laser frequency over a cavity resonance and measuring the transmitted intensity with a photodetector. A fit of the transmission spectrum with a function based on mode-coupling theory[14] then allows to determine the intrinsic cavity quality factor (i.e., without loading loss). More details on coupling and tapered fiber fabrication can be found in Refs. 8, 15, and 16.

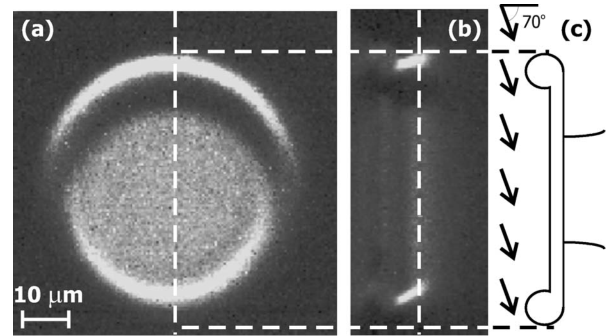

FIG. 3. Confocal PL microscopy images ($\lambda = 1540$ nm) of a postimplanted microtoroid. (a) *x-y* PL cross section, with the vertical line indicating the location of the *x-z* cross section shown in (b). (b) *y-z* PL cross section, with the vertical line indicarting the location of the cross section shown in (a). (c) *x-z* outer perimeter of the microtoroid determined from spatially imaged Rhodamine PL. Also indicated is the implantation angle of 70°.

III. RESULTS

A. Confocal photoluminescence spectroscopy

1. Postimplanted microtoroids

Figure 3 shows two-dimensional cross sections of the Er PL distribution in a postimplanted microtoroid implanted to a fluence of 4.2×10^{15} Er/cm^2. Integrated intensity in the wavelength range of 1520–1565 nm is plotted, corresponding to the $^4I_{13/2} \rightarrow {}^4I_{15/2}$ transition of Er^{3+}. Figure 3(a) shows the *x-y* PL cross section [taken at the *z* position indicated by the vertical line in Fig. 3(b)]. With a subsequent measurement, at the same position, of the two-dimensional distribution of the Rhodamine PL in the visible (not shown) the outer perimeter of the microtoroid was estimated, as is shown in Fig. 3(c). The toroid's major diameter is 57 μm; the minor diameter is 6 μm. Also indicated is the direction of the Er ion implantation, at an angle of 70° relative to the surface normal. As can be seen in Fig. 3(a), the implantation results in a very inhomogeneous Er distribution along the circumference of the microtoroid. At the side facing the ion beam, Er ions are located near the outer perimeter of the microtoroid. At the opposite side, where the toroidal ring protrudes upwards, the Er ions are located at the inner perimeter. Clear "shadowing" effects can be observed at the sides of the ring that face away from the ion beam direction, which is due to the finite projected range of the Er ions. The inner region of planar SiO_2 shows Er PL, albeit at a lower intensity, due to the fact that the Er ion fluence is geometrically reduced by the oblique angle of incidence [by cos(70°)].

Figure 3(b) shows the *x-z* infrared Er PL cross section [image plane taken along the vertical line indicated in Fig. 3(a)]. Again this image shows that on the side facing the ion beam, the Er ions are located at the outer perimeter of the toroidal ring in contrast to the side opposite the ion beam, where the Er ions are located at the inner perimeter of the toroidal ring. Also the inclination of the ion beam with respect to the sample can be observed from the Er PL distribution at the outer perimeter; it is approximately 70°, in agreement with the implantation angle. A slightly different angle is observed at the inner perimeter, which is attributed to a different curvature of the toroidal surface at the inner perimeter. From these images we can conclude that the Er

Downloaded 12 Jun 2006 to 192.87.154.163. Redistribution subject to AIP license or copyright, see http://jap.aip.org/jap/copyright.jsp

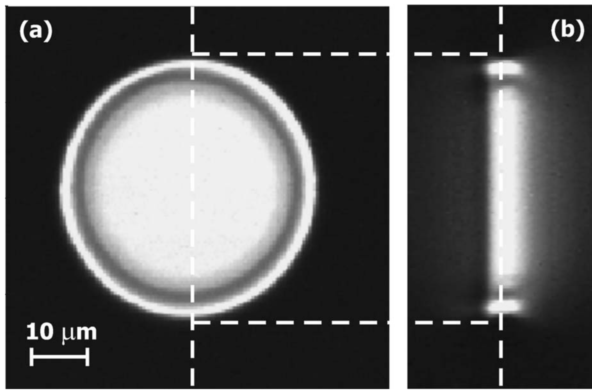

FIG. 4. Confocal PL microscopy images (λ=1540) of a preimplanted microtoroid. (a) *x-y* cross section, with vertical line indicating the location of the *x-z* cross section shown in (b). (b) *x-z* cross section, with the vertical line indicating the location of the cross section shown in (a).

ions are indeed distributed as expected from the implantation energy and angle, and that optical activation of the Er ions through the entire implanted section of the microtoroid is achieved.

2. Preimplanted microtoroids

Figure 4 shows the two-dimensional confocal infrared PL cross sections of a microtoroid preimplanted with 1.2×10^{16} Er/cm^2. Figure 4(a) shows the *x-y* PL cross section of this microtoroid [image plane taken at the *z* position indicated by the vertical line in Fig. 4(b)]. Figure 4(b) shows the *x-z* PL cross section [image plane along the vertical line indicated in Fig. 4(a)]. The microtoroid's outer diameter is 57 μm and the minor diameter is 6 μm. It is clear that Er is optically activated throughout the entire toroidal ring. The cylindrically symmetric PL distribution is in agreement with the fabrication procedure. Given the resolution of Er PL mappings described in Sec. II B it is difficult to determine the precise location of Er ions in the toroidal structure. The distribution of Er ions in the preimplanted microtoroids is the result of a complex process where Er is first implanted in a planar film and then the laser reflow is used to form the microtoroid. In contrast to the postimplanted microtoroids, the reflow process results in an unknown roll-up/collapse process and may also cause Er diffusion in the formed structure, leading to an unknown Er doping profile. Therefore, μRBS was used to investigate this further.

B. Microprobe Rutherford backscattering spectrometry

Figure 5 schematically shows two different Er doping models for preimplanted microtoroids. Figure 5(a) shows the most simple reflow model; the structure has rolled up into a ring and, due to thermal diffusion, the microtoroid is homogeneously doped with Er. In this model it is assumed that during the laser reflow of the SiO_2, the temperature-time profile is such that Er can diffuse over large distances. Figure 5(b) shows an alternative model where the Er ions do not diffuse. They are immobile relative to the SiO_2 and thus follow the plastic deformation of the SiO_2 that has rolled upwards to form the microtoroid's ring. To distinguish between the different Er distribution models we measured the Er depth profile spatially resolved on the microtoroid made from 1 μm thick SiO_2 and preimplanted with 300 keV Er.

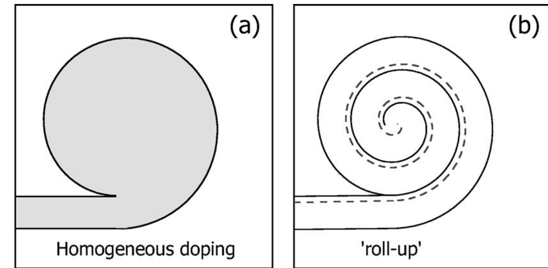

FIG. 5. Two different models for the Er distribution in preimplanted microtoroids. (a) Erbium is homogeneously diffused through the entire toroidal ring. (b) Er is not diffused, the SiO_2 is rolled up, and the Er is located far from the top surface.

Figures 6(a) and 6(b) show the SEM images taken from the side of the microtoroid after the μRBS measurement. The periodic raster of the μRBS beam can be clearly observed on the top surface. However, no damage or large-scale deformation of the structure can be observed in either image.[17] Figure 6(c) shows a spatial image of the backscatter yield, integrated over all energies. The detector is located at the topside of the microresonator structure, giving rise to a shadowing effect at the bottom of the image (i.e., backscattered He^+ ions from that region cannot reach the detector). The top part of the scan has a higher total backscatter yield than the bottom part, a feature that we attribute to the close vicinity of the detector to this side, resulting in a larger detection solid angle.

To obtain detailed information of the Er distribution in both the toroidal ring and the planar inner circle region, μRBS spectra were integrated and summed for both areas. Identification of the pixels belonging to the toroidal ring and inner circle was based on the image in Fig. 6(c). Figure 7 shows these spatially summed μRBS spectra for both areas. The spectra are normalized to the number of pixels over which they were collected. Figure 7(a) shows the integrated RBS spectrum for the inner circle section of the microtoroid [see Fig. 6(a)]. The peak at 1810 keV corresponds to backscattering from Er ions at a depth of 110 nm; the arrow indicates the Er surface channel. An identical depth profile (not

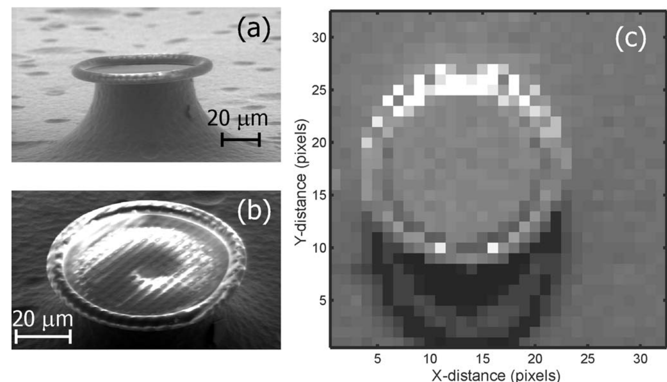

FIG. 6. [(a) and (b)] Side view SEM images of the microtoroid that was investigated with μRBS. (c) Spatial image of the integrated μRBS yield from the microtoroid presented in (a) and (b).

Downloaded 12 Jun 2006 to 192.87.154.163. Redistribution subject to AIP license or copyright, see http://jap.aip.org/jap/copyright.jsp

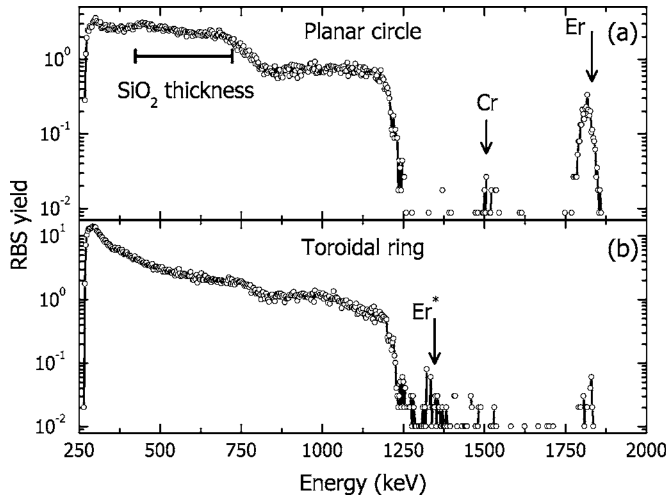

FIG. 7. (a) RBS spectrum with counts integrated from the inner circle section of the microtoroid. Indicated is the thickness of the SiO_2 layer. The horizontal arrow indicates the energy difference that corresponds to an SiO_2 thickness of 833 nm. (b) RBS spectrum with counts integrated from the toroidal ring section of the microtoroid.

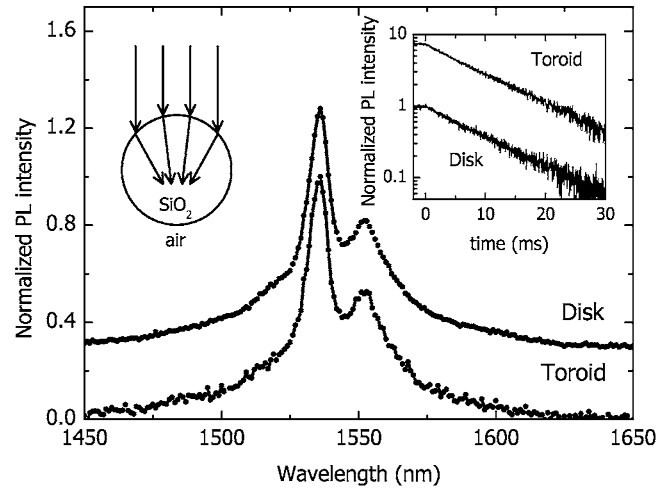

FIG. 8. Measured Er PL emission spectra of a preimplanted microtoroid and a microdisk. Inset on the right shows the PL decay measured at the Er peak emission wavelength. Both samples have the same decay rate. Schematic on the left shows refraction of excitation light on the toroidal ring. Er ions close to the outer sides of the ring are inefficiently excited.

shown) was measured on a planar reference sample (without laser reflow). This indicates that Er ions do not diffuse in the silica inner circle upon laser reflow. Note that due to thermal conduction to the Si substrate during the laser pulse, the peak temperature in the inner circle is lower than in the outer ring. PIXE measurements showed the presence of Cr and Er on the inner circle, the former is reflected by the low intensity peak at 1510 keV occurring at the surface channel of Cr (indicated). We attribute the presence of Cr to contamination of the initial wafer by the use of the optical lithography mask in the fabrication process.[9] The spectrum also shows the Si and O surface channels at 1225 and 720 keV, respectively. For this sample and RBS geometry, the O surface edge overlaps with the surface channel from the Si substrate under the SiO_2, and is therefore difficult to discern. The reduction in O signal below 420 keV is due to the finite width of the SiO_2 layer, indicated by the horizontal bar. A simulation of the multilayer structure gave an estimate for the SiO_2 areal density of 5.5×10^{18} at./cm^2, corresponding to 833 nm, somewhat smaller than the 1 μm oxide thickness of the starting material.

Figure 7(b) shows the summed RBS spectrum for the toroidal ring section of the microtoroid. The Er at the surface of the microtoroid is almost completely absent due to the upwards roll up of the SiO_2 disk. The few Er counts at 1810 keV are due to the width of the microprobe beam, thereby also probing small sections of the inner circle region. Interestingly, a small peak can be observed in the spectrum at 1340 keV (indicated by Er*) that is not observed for the inner circle region in Fig. 7(a). The energy of this Er peak corresponds to the location of the Er at the back of the rolled-up 1 μm SiO_2 layer, in agreement with model shown in Fig. 5(b).

The absence of Er diffusion upon laser reflow is in agreement with an extrapolation of RBS measurements of thermally annealed Er-implanted SiO_2 reported in Ref. 18. It was found that Er depth profiles before and after annealing for 1 h at 1200 °C showed no substantial diffusion. The Er diffusion length is then estimated to be smaller than 10 nm. Using an activation energy of 3.5 eV (a typical value for diffusion in amorphous materials), a laser anneal time of 1 ms (typical laser pulse duration), and an estimated temperature of 2000 K, the calculated diffusion length is smaller than 10 nm, in agreement with our μRBS depth profiling measurements.

For both types of Er-implanted microtoroids we have determined the distribution of optically active Er ions, information that is crucial in analyzing the optical measurements that follow.

C. Time-resolved photoluminescence spectroscopy

We measured the Er PL emission in a preimplanted microtoroid and in a microdisk (after step 6 in Fig. 1, no laser reflow) both located on the same Si chip and implanted with 4.2×10^{15} Er/cm^2. The structures are excited from the top with 488 nm laser light and the PL is collected from the top. Figure 8 shows the Er PL emission spectra. Both samples show characteristic Er PL emission peaking at 1536 nm. No additional structure in the PL emission spectrum (due to coupling of Er ions to cavity modes) is visible. Indeed, PL emitted perpendicular to the sample is mainly due to spontaneous emission into the far field and is not affected by coupling to cavity modes. Er emission coupled to cavity modes emanates preferentially in the plane of the microdisk/toroid and is not probed in this experiment.[19] PL lifetimes were measured at the peak Er emission wavelength. Both microtoroid and microdisk show a similar lifetime of 10.5 ms. This lifetime is substantially shorter than the radiative lifetime of 18 ms for Er ions in thermal SiO_2.[20] We attribute this to concentration quenching processes that, through resonant energy transfer between Er ions, causes quenching of excited Er ions due to coupling to OH impurities in the SiO_2. Using a linear concentration quenching model[21] with $C_{\mathrm{Er,Er}}=2.9\times10^{-39}$ cm^6/s (Ref. 22) we obtain an OH concentration of

Downloaded 12 Jun 2006 to 192.87.154.163. Redistribution subject to AIP license or copyright, see http://jap.aip.org/jap/copyright.jsp

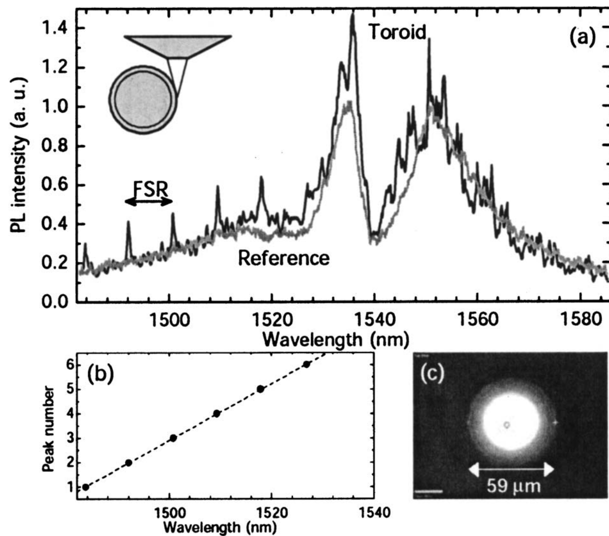

FIG. 9. (a) Er PL emission spectra collected from the side of the microtoroid (black line) and from the top of a planar section of the microtoroid (gray line). The inset shows a side view of the experimental geometry. (b) Peak number of the PL enhancement observed in (a) vs peak wavelength. (c) Top view optical microscopy image of the microtoroid, its diameter is indicated.

7.5×10^{18} cm^{-3}, indeed a much lower concentration than the peak Er concentration, thereby validating the linear concentration quenching model. Assuming an OH absorption cross section of 3.5×10^{-24} cm^2 (estimated from absorption measurements in glass fibers,[23] we obtain an OH absorption-related $Q=5.2\times10^8$. This would then be an upper limit on the Q that can be attained in these microcavities fabricated from thermal SiO_2. The fact that similar Er PL lifetimes were observed before and after laser reflow further supports the conclusion that no significant Er diffusion has taken place. If it had, the Er concentration would have lowered, resulting in less concentration quenching, and thus a longer Er lifetime for the microtoroid after reflow, contrary to what is observed.

Note that in this analysis we disregarded any influence of the cavity on the lifetime of the Er ions. There are two reasons for this. First, using far-field excitation only a very small fraction of the probed Er ions have substantial overlap with high-Q modes. Due to refraction at the SiO_2/air interface, as sketched in the inset on the left in Fig. 8, we expect that Er ions close to the outer perimeter of the microcavity (that can couple efficiently to the high-Q modes) are not efficiently excited. Erbium ions are excited mainly in the center of the toroidal ring and in the planar SiO_2 where coupling to cavity modes is inefficient. Second, even for the high-Q modes, Purcell enhancement of the spontaneous decay rate is not expected in erbium at room temperature owing to the large homogeneous linewidth of individual Stark-split transitions.[24]

By using the confocal microscope PL setup, described in Sec. II B, we can selectively excite Er ions in the microtoroid that couple to cavity modes. The preimplanted microtoroid [see Fig. 9(c)] was mounted sideways under the microscope objective (60×). A small pump beam was focused through the objective on the near-surface region of the microtoroid, tangentially to the perimeter [see inset on the left in Fig. 9(a), showing a side view schematic], Er ions were locally excited and their PL emission spectrum was collected in the plane of the microtoroid through the same objective [black line in Fig. 9(a)]. A series of periodic peaks, superimposed on the slowly varying Er emission, can be clearly observed. As a reference, an Er PL emission spectrum was measured from the top of a planar section of the same sample (gray line); it does not show the sharply peaked periodic modulation. The enhancements in Er PL are attributed to an enhanced optical density of states at the cavity resonances that lead to an increase of the Er spontaneous emission into these cavity modes. Due to the finite Q, the fields associated with these modes leak and scatter out of the cavity, preferentially in the plane of the microtoroid, and are collected by the microscope objective (see also Ref. 19). The linewidths of the Er PL enhancements [not limited by detector resolution ($Q<15000$)] correspond to Q factors in the order of 1500, significantly lower than the Q factors obtained from tapered fiber transmission measurements on the same samples before implantation (typically 10^8). This suggests that the probed Er ions couple to low-Q modes. As can be seen in Fig. 9(a) a large fraction of the detected Er emission is not influenced by the microcavity. This is in agreement with the μRBS measurements that show that Er ions are located far from the microtoroid's perimeter. In that case the probed Er ions do not couple efficiently to high-Q cavity modes (that have their field maxima close to the toroid's perimeter), but rather couple to low-Q higher-order radial modes. Note that the overall shape of the Er emission spectra in Fig. 9(a) is different from that generally observed for Er in SiO_2.[18] Since both measurements have a pronounced dip at $\lambda=1540$ nm this is attributed to an interference effect in the confocal microscopy setup.

After normalizing the cavity modified Er emission spectrum with the reference spectrum, the periodic peaks are more easily identifiable. Figure 9(b) shows the peak number versus peak wavelength, which is fitted with a linear equation showing that the peaks have an equidistant spacing. The slope results in a free spectral range (FSR) of 8.6 nm. The angular FSR (expressed in wavelength) is approximated by

$$FSR_\lambda = \frac{\lambda^2}{2\pi R n_{\mathrm{eff}}}, \tag{1}$$

with R the major radius of the toroid and n_{eff} is the effective mode index. Using Eq. (1) and $n_{\mathrm{eff}}=1.45$ we obtain a radius of 29.4 μm, close to the radius of 29.5 μm obtained from optical microscopy imaging [Fig. 9(c)], further proving that the observed peaks are related to whispering gallery cavity modes. In this analysis we assumed a dispersionless refractive index (which is a good approximation for infrared wavelengths in SiO_2) and the optical mode fully confined to the microtoroid (i.e., $n_{\mathrm{eff}}=n_{SiO_2}$).

To investigate the relation between cavity modes and Er emission into these modes in more detail, we directly compared tapered fiber transmission measurements on the same microtoroid as shown in Fig. 9. Figure 10(b) shows a section of the mode spectrum obtained from the PL measurement presented in Fig. 9(a). The Er PL was normalized with the reference PL measurement. Figure 10(a) shows the transmission spectrum of the same microtoroid measured using a

Downloaded 12 Jun 2006 to 192.87.154.163. Redistribution subject to AIP license or copyright, see http://jap.aip.org/jap/copyright.jsp

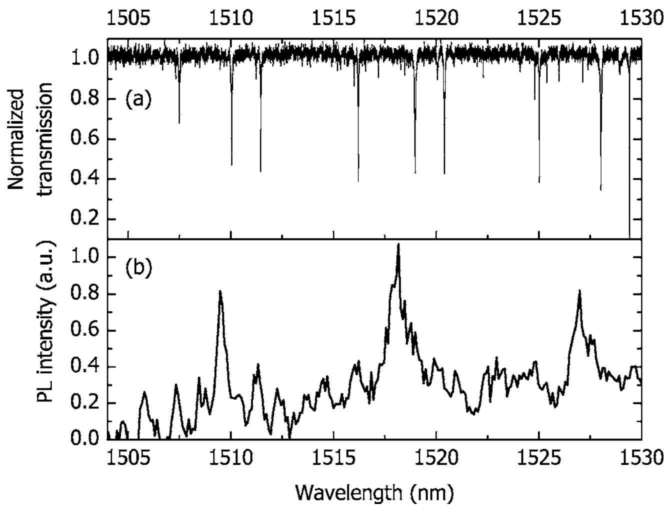

FIG. 10. (a) Normalized transmission spectra measured through a tapered optical fiber measured in close proximity to the microtoroid. (b) Relative Er PL intensity obtained from Fig. 9(a).

tapered optical fiber in the undercoupled regime. Note that with this method we preferentially excite high-Q, low-order modes, which have their field maxima located close to the perimeter of the microtoroid. It can be observed that the modes, now seen as dips in the fiber transmission spectra, occur at different wavelengths than the modes obtained from the Er PL measurements. Also it is clear that the modes measured in transmission have a much smaller linewidth (by ca. three to four orders of magnitude). However, both measurements show nearly the same angular free spectral range of 8.6 nm. These data confirm that the probed Er ions preferentially couple to low-Q whispering gallery modes.

D. Microtoroid quality factors

We determined the intrinsic Q factors (i.e., not affected by the coupling) for both postimplanted and preimplanted microtoroids. Figure 11 shows a characteristic transmission spectrum measured through the tapered optical fiber around $\lambda = 1442$ nm on a postimplanted microtoroid. The transmission spectrum was fitted with a function derived from mode-coupling theory,[14] and from this fit an intrinsic $Q = 1.6 \times 10^7$ was determined. A similar measurement on a preimplanted microtoroid yielded $Q = 3.9 \times 10^7$. To compare Q's for preimplanted and postimplanted microtoroids, the Er concentration profile in the microtoroid, probe wavelength, and mode profiles have to be taken into account.

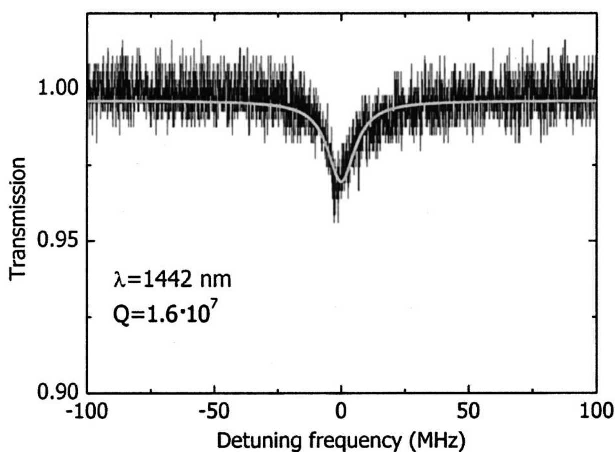

FIG. 11. Fiber taper transmission spectrum of a postimplanted microtoroid (black) measured around $\lambda = 1442$ nm. From the fit (gray) an intrinsic Q of 1.6×10^7 was derived.

Using the known implantation profile, the mode overlap Γ was calculated using

$$\Gamma = \frac{(1/\mathrm{Er}_{\max}) \int_A \mathrm{Er}(x,y) I(x,y) dA}{\int_A I(x,y) dA}, \tag{2}$$

with A being a large surface cutting perpendicular through the toroidal ring, $\mathrm{Er}_{\max}$ the peak Er concentration, $\mathrm{Er}(x,y)$ the position-dependent Er distribution, and $I(x,y)$ the optical mode intensity distribution. The spatial optical mode distribution was calculated with a finite element method[25] for a postimplanted microtoroid (major diameter of 57 μm and minor diameter of 6 μm) and preimplanted microtoroid (major diameter of 25 μm and minor diameter of 2.5 μm, as estimated from the SEM image in Ref. 26. These mode profiles were then fitted with a double-Gaussian function, which was used as an input for the overlap calculation using Eq. (2). The Er doping profiles were calculated with the projected range and straggle of the Er ions as inputs.

Due to the absence of cylindrical symmetry for postimplanted microtoroids the mode overlap of Eq. (2) was calculated for a series of toroidal cross sections at different angles. These where then integrated over all angles and appropriately averaged to obtain the average overlap. The resulting mode overlap was $\Gamma = 0.066$. The mode overlap for the preimplanted microtoroid was calculated with a Gaussian Er distribution located in the center of the toroidal ring (according to the μRBS the Er should be located at 1.9 μm below the surface, but the small minor diameter of the ring suggests that significant ablation of SiO_2 has taken place and the Er was therefore assumed to be located in the center of the ring). Due to the cylindrical symmetry the overlap Γ was calculated only over the toroidal ring's cross section A. The calculated mode overlap was $\Gamma = 0.02$.

The Er absorption-related Q's can be calculated for the weak pump regime (i.e., no significant excited state population) with[25]

$$Q = \frac{2\pi n}{N_0 \Gamma \sigma_a \lambda} \tag{3}$$

with n as the refractive index, Γ as the mode overlap, N_0 as the peak Er concentration, and σ_a as the Er absorption coefficient at the probe wavelength. From the transmission spectrum for a postimplanted microtoroid measured around $\lambda = 1442$ nm, shown in Fig. 11, an intrinsic Q factor of 1.6×10^7 was derived. Given the values $\Gamma = 0.066$, N_0 calculated for the implanted Er fluence of 4.2×10^{15} cm^{-2}, $\sigma_a = 4 \times 10^{-22}$ cm^2 at 1442 nm,[27] we obtain an Er absorption-related $Q = 1.6 \times 10^7$, equaling the Q obtained from the transmission experiments. For preimplanted microtoroids that were probed at $\lambda = 1411$ nm,[26] we used an Er absorption

Downloaded 12 Jun 2006 to 192.87.154.163. Redistribution subject to AIP license or copyright, see http://jap.aip.org/jap/copyright.jsp

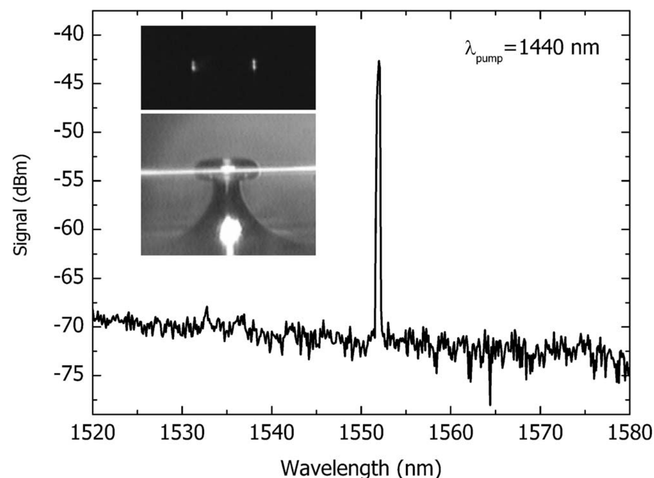

FIG. 12. Erbium lasing spectrum for a postimplanted microtoroid pumped at λ=1440 nm. The top inset shows a side view image of the microtoroid, showing green Er upconversion luminescence when pumped at high pump powers (printed in black and white). The bottom inset shows a CCD camera image of the measurement geometry.

cross section of $\sigma_a = 1 \times 10^{-22}$ cm^2,[27] N_0 calculated for the Er fluence of 4.2×10^{15} cm^{-2}, and the calculated overlap $\Gamma = 0.02$ and obtain an Er absorption-related $Q = 1.8 \times 10^8$, in reasonable agreement with the experimentally determined $Q = 3.9 \times 10^7$. We therefore conclude that for both post- and preimplanted microtoroids the measured Q's are for a large part determined by Er absorption.

E. Erbium microtoroid lasing

Both types of Er-doped microtoroids showed lasing at 1.5 μm when pumped at a power above their lasing threshold. Postimplanted microtoroids were pumped at 1440 nm and showed single or multimode mode lasing around 1552 nm. The lowest obtained lasing threshold in these microtoroids was 125 μW (power launched into the fiber). Figure 12 shows the Er lasing spectrum for the postimplanted microtoroid obtained by pumping at 800 μW. When pumped at such high powers intense green emission was observed (see top inset in Fig. 12). This is related to population of higher Er^{3+} energy levels by a combination of cooperative upconversion processes[28] and excited state absorption.[29] Whether the observed green emission is due to spontaneous emission from the excited higher energy levels of Er or is in fact due to lasing, must be further investigated.

The preimplanted microtoroids showed much lower Er lasing thresholds as was shown and analyzed in more detail in Ref. 26. In summary, both single and multimode lasings were observed (depending on the pump power). The lowest measured lasing threshold was 4.5 μW of launched pump power for a microtoroid with a major diameter of 25 μm and with a $Q = 3.9 \times 10^7$. The preimplanted microtoroids also showed green upconversion luminescence when pumped at powers far above their lasing threshold.

For both post- and preimplanted microtoroids, the Er absorption-related Q has the same order of magnitude as the measured intrinsic Q. Therefore the effect of intrinsic losses are small and the lasing threshold is largely determined by the power required to invert the Er ions. It thus depends only on the Er concentration, the absorption and emission cross sections, the modal volumes, and the overlap of the signal and pump wavelengths with the Er distribution. We attribute the much lower lasing threshold for preimplanted microtoroids to the much smaller mode volume [the major diameter is 25 μm versus 57 μm, corresponding to a mode volume ratio of ~6 (Ref. 30).

IV. CONCLUSIONS

Erbium-doped SiO_2 toroidal microcavity lasers on a Si substrate were made. Two fabrication techniques were compared: one where Er is implanted in the SiO_2 base material and one where Er is implanted in a fully fabricated microcavity. Confocal PL spectroscopy imaging shows distinctly different distributions of optically active Er in the two types of microtoroids. From microprobe RBS it is concluded that Er does not diffuse during the laser reflow. From the measured Er distribution and calculated mode profiles the mode overlap factors were calculated. It was found that cavity losses in both types of Er-doped microcavities are dominated by Er absorption. Single-mode lasing is observed for both types of cavities, with the lowest threshold found for the cavity with smallest mode volume. When Er ions are selectively excited using confocal microscopy, a well-defined mode spectrum is observed superimposed on the far-field luminescence spectrum.

ACKNOWLEDGMENTS

Leo IJzendoorn and Peter Mutsaers are thanked for their help with the μRBS measurements. The Dutch part of this work is part of the research program of the "Stichting voor Fundamenteel Onderzoek der Materie (FOM)," which is financially supported by the "Nederlandse organisatie voor Wetenschappelijk Onderzoek (NWO)." One of the authors (A.T.) is grateful to Funds of NATEQ (Québec, Canada) for postdoctoral scholarship. Research at the California Institute of Technology was funded by the DAPRA, the NSF, and the Caltech Lee Center for Advanced Networking.

[1] K. J. Vahala, Nature (London) **424**, 839 (2003).
[2] M. T. Hill, *et al.*, Nature (London) **432**, 206 (2004).
[3] P. Rabiei, W. H. Steier, C. Zhang, and L. R. Dalton, J. Lightwave Technol. **20**, 1968 (2002).
[4] K. Srinivasan, P. E. Barclay, O. Painter, J. Chen, A. Y. Cho, and C. Gmachl, Appl. Phys. Lett. **83**, 1915 (2003).
[5] D. W. Vernooy, V. S. Ilchenko, H. Mabuchi, E. W. Streed, and H. J. Kimble, Opt. Lett. **23**, 247 (1998).
[6] V. B. Braginsky, M. L. Gorodetsky, and V. S. Ilchenko, Phys. Lett. A **137**, 393 (1992).
[7] V. Sandoghdar, F. Treussart, J. Hare, V. Lefèvre-Seguin, J.-M. Raimond, and S. Haroche, Phys. Rev. A **54**, R1777 (1996).
[8] M. Cai, O. Painter, K. J. Vahala, and P. C. Sercel, Opt. Lett. **25**, 1430 (2000).
[9] D. K. Armani, T. J. Kippenberg, S. M. Spillane, and K. J. Vahala, Nature (London) **421**, 925 (2003).
[10] A. Polman, B. Min, J. Kalkman, T. J. Kippenberg, and K. J. Vahala, Appl. Phys. Lett. **84**, 1037 (2004).
[11] T. J. Kippenberg, S. M. Spillane, D. K. Armani, and K. J. Vahala, Opt. Lett. **29**, 1224 (2004).
[12] T. J. Kippenberg, S. M. Spillane, and K. J. Vahala, Phys. Rev. Lett. **93**, 083904 (2004).
[13] J. F. Ziegler, J. P. Biersack, and U. Littmark, *The Stopping and Range of Ions in Solids* (Pergamon, New York, 1985).

Downloaded 12 Jun 2006 to 192.87.154.163. Redistribution subject to AIP license or copyright, see http://jap.aip.org/jap/copyright.jsp

[14]H. A. Haus, *Waves and Fields in Optoelectronics* (Prentice-Hall, Englewood Cliffs, 1984).
[15]S. M. Spillane, T. J. Kippenberg, O. J. Painter, and K. J. Vahala, Phys. Rev. Lett. **91**, 043902 (2003).
[16]J. C. Knight, G. Cheung, F. Jacques, and T. A. Birks, Opt. Lett. **22**, 1129 (1997).
[17]T. van Dillen, A. Polman, C. M. van Kats, and A. van Blaaderen, Appl. Phys. Lett. **83**, 4315 (2003).
[18]A. Polman, J. Appl. Phys. **82**, 1 (1997).
[19]J. Verbert, F. Mazen, T. Charvolin, E. Picard, V. Calvo, P. Noé, J.-M. Gérard, and E. Hadji, Appl. Phys. Lett. **86**, 111117 (2005).
[20]M. J. A. de Dood, L. H. Slooff, A. Moroz, A. van Blaaderen, and A. Polman, Phys. Rev. A **64**, 033807 (2001).
[21]M. J. Weber, Phys. Rev. B **4**, 2932 (1971).
[22]J. Kalkman, L. Kuipers, A. Polman, and H. Gersen, Appl. Phys. Lett. **86**, 041113 (2005).
[23]S. R. Bickham and M. B. Cain, in *Undersea Fiber Communications Systems*, edited by J. Chesnoy (Academic, San Diego, 2002).
[24]J. L. Zyskind, E. Desurvire, J. W. Sulhoff, and D. DiGiovanni, IEEE Photonics Technol. Lett. **2**, 869 (1990).
[25]S. M. Spillane, T. J. Kippenberg, K. J. Vahala, K. W. Goh, E. Wilcut, and H. J. Kimble, Phys. Rev. A **71**, 013817 (2005).
[26]B. Min, T. J Kippenberg, L. Yang, K. J. Vahala, J. Kalkman, A. Polman, Phys. Rev. A **70**, 033803 (2004).
[27]P. C. Becker, N. A. Olsson, and J. R. Simpson, *Erbium-Doped Fiber Amplifiers: Fundamentals and Technology* (Academic, San Diego, 1997).
[28]E. Snoeks, G. N. van den Hoven, A. Polman, B. Hendriksen, M. B. J. Diemeer, and F. Priolo, J. Opt. Soc. Am. B **12**, 1468 (1995).
[29]W. J. Miniscalco, J. Lightwave Technol. **9**, 234 (1991).
[30]T. J. Kippenberg, S. M. Spillane, and K. J. Vahala, Appl. Phys. Lett. **85**, 6113 (2004).

Downloaded 12 Jun 2006 to 192.87.154.163. Redistribution subject to AIP license or copyright, see http://jap.aip.org/jap/copyright.jsp